RSC Advances

ROYAL SOCIETY OF CHEMISTRY

www.rsc.org/advances

Improved electrochemical performances of layered lithium rich oxide $0.6Li[Li_{1/3}Mn_{2/3}]O_2$ $0.4LiMn_{5/12}Ni_{5/12}Co_{1/6}O_2$ by Zr doping

Zheng Ma [a], Jichun Huang [a], Jingbin Quan [a], Lin Mei [a], Jun Guo [b],

Decheng Li [a*]

[a] College of Physics, Optoelectronics and Energy & Collaborative Innovation Center of Suzhou Nano Science and Technology, Soochow University, Suzhou 215006, China

[*] E-mail: lidecheng@suda.edu.cn; Fax: +86-512-67261575; Tel: +86-512-67261337

[b] Testing and analysis center, Soochow University, Suzhou 215006, China

Abstract: A series of layered lithium-rich oxides $0.6Li[Li_{1/3}Mn_{2/3(1-x)}Zr_{2/3x}]O_2$ $0.4LiMn_{5/12}Ni_{5/12}Co_{1/6}O_2$ ($0 \leq x \leq 10\%$) have been prepared by spray-dry method. The crystal structural and morphological properties of all samples have been studied by XRD, XPS, SEM, HRTEM and SAED. XRD results reveal Zr^{4+} ions are doped into the lattice. HRTEM results suggest Zr^{4+} ions can stabilize the layered structural feature during cycles. The electrochemical properties are remarkably upgraded by Zr^{4+} ions doping. The discharge capacity of Zr4% doped samples remains 218.9 mA h g^{-1} after 100 cycles with a capacity retention of 84% at 20 mA g^{-1} between 2.0 and 4.8 V, while the undoped samples drop to 168.6 mA h g^{-1} with a capacity retention of 72%. Moreover, Zr4% doped samples show the lowest voltage decay, about 0.16 V lower than the undoped samples after 100 cycles. This

study suggests suitable Zr^{4+} doping can improve the electrochemical performances and suppress voltage decay for layered lithium-rich oxides.

1. Introduction

With the development of economics, rechargeable lithium-ion batteries (LIBs) have been considered as the most promising power sources in the field of hybrid electric vehicles (HEVs) and electric vehicles (EVs) [1-3] due to their high energy density, light weight, and long cycle life. Recently, lithium-rich solid-solution layered oxides, which could be denoted as $xLi_2MnO_3 \cdot (1-x)LiMO_2$ (M = Mn, Co, Ni) [4, 5], have been the focus of intense research since they can deliver a higher reversible capacity (ca. 250 mA h g^{-1}) or more at low cost compared with the commercialized cathode materials such as $LiCoO_2$, $LiFePO_4$, $LiMn_2O_4$ and $LiMn_{1/3}Ni_{1/3}Co_{1/3}O_2$ [6-10].

However, several major problems still exist for these lithium-rich layered oxides. For example, a large irreversible capacity loss in first charge/discharge cycle, severe capacity fading, poor rate capability and voltage decay during subsequent charge-discharge cycles, all of which limits its commercialization [11-16]. These issues are closely related to the reaction mechanism of the layered Li-rich cathode materials. As to the reaction mechanism, it has been extensively studied. In general, $xLi_2MnO_3 \cdot (1-x)LiMO_2$ (M = Mn, Co, Ni) can be considered as two components Li_2MnO_3 ($Li[Li_{1/3}Mn_{2/3}]O_2$) and $LiMO_2$ with a layered structure on the basis of hexagonal a-$NaFeO_2$. It is known that Li_2MnO_3 is electrochemically inactive between

2 and 4.4 V in its crystalline structure. When charged beyond 4.4 V, lithium can deintercalate from the Li_2MnO_3 component with a release of oxygen removing Li_2O or oxygen gas evolution [17]. It was reported non-removable Ni^{2+} can occupy the Li layer during the first charge process, resulting in irreversible structural rearrangements called ‘‘cation mixing’’ [18] and a large irreversible capacity loss. Moreover, this process partly reduced the Mn ions from the tetravalent to trivalent state when discharged after charging to a high voltage plateau (> 4.4 V) [19], which dissolved the Mn^{3+} ions in the electrolyte. It was known this can form a thick solid-electrolyte interface (SEI) in the cathode surface, resulting in severe capacity fading, poor rate capability and voltage decay during subsequent charge-discharge cycles.

Many efforts have been made to overcome the above problems, such as surface modification on the particles with ZrO_2 [20], MgO [21], CaF_2 [22], aiming at avoiding the reaction between cathode surface and the electrolyte even at a high cut-off voltage. Although this method can enhance the cycling stability and keep good rate capability, it is still hard to eliminate the irreversible capacity loss completely. Foreign ions doping into the layered lattice of lithium-rich oxides are another method. Many kinds of ions like Ru [23, 24], Mg [25], Fe [26], Mo [27, 28], Y [29], Ti [30], F [31] were chosen, which can effectively improve electrical conductivity and structure stability. Recently, S. Kang et al have reported suitable Y substitution can influence the voltage decay [29]. Moreover, S. Wang et al have proved Ti substitution for Mn in Li_2MnO_3 can suppress the voltage decay [32], which means doping suitable atoms is important to suppress the voltage decay. Unfortunately, this improvement could not completely

suppress the voltage decay during subsequent charge-discharge cycles.

In this paper, Zr^{4+} was selected as a dopant to substitute for Mn^{4+}. It is believed that monoclinic Li_2ZrO_3 is isomorphous to Li_2MnO_3 (C2/c). And Zr^{4+} ions (rZr^{4+} = 0.072 nm) has bigger size, stronger Zr-O bond than Mn^{4+} ions (rMn^{4+} = 0.053 nm). Meanwhile, Zr^{4+} ions can compensate the charge loss of oxygen because it does not involve in oxidation/reduction reactions. Therefore, $0.6Li[Li_{1/3}Mn_{2/3(1-x)}Zr_{2/3x}]O_2$ $0.4LiMn_{5/12}Ni_{5/12}Co_{1/6}O_2$ ($0 \leq x \leq 10\%$) composite cathode materials were prepared and characterized by structure, morphology and electrochemical performances.

2. Experimental

2.1. Sample preparation

Lithium-rich layered oxides $0.6Li[Li_{1/3}Mn_{2/3(1-x)}Zr_{2/3x}]O_2$ $0.4LiMn_{5/12}Ni_{5/12}Co_{1/6}O_2$ ($0 \leq x \leq 10\%$) were prepared by a spray-dry method following a typical synthesis route. Stoichiometric amounts of $LiOH \cdot H_2O$ (5% excess of lithium to compensate for evaporative lithium loss), $Ni(CH_3COO)_2 \cdot 4H_2O$, $Co(CH_3COO)_2 \cdot 4H_2O$, $Mn(CH_3COO)_2 \cdot 4H_2O$ and $Zr(CH_3COO)_2$ were dissolved in deionized water and then added critic acid (chelating agent) into aqueous solutions, afterwards we received well mixed powder by spray-dry process. Then the powders were calcined at 900 ℃ for 25 s to quickly remove the organic residue, subsequently grounded and pressed into pellets, before being sintered at 900 ℃ for 12 h in air in a muffle furnace. After that, the calcined pellets were quickly quenched in liquid nitrogen to obtain the final

samples.

2.2. Structure characterization

The crystal structure of samples were detected by x-ray diffraction (XRD) with Cu-Kα radiation operated at 40 kV and 40 mA, which was recorded at a scan rate of $4^\circ\ min^{-1}$ in the 2θ range of 10-80°. The particle morphologies of samples were observed by a SU8010 scanning electron microscope (SEM) working at an acceleration voltage of 10 kV. To get more microstructure information of samples, high resolution transmission electron microscope (HRTEM) (FEI-Tecnai G2 F20 S-TWIN) and selected area electron diffraction (SAED) were performed at an acceleration voltage of 200kV. The valence states of Ni, Co, and Mn, Zr ions in the samples were tested on ESCA-LAB 250Xi apparatus with Al Kα X-ray source by X-ray photoelectron spectroscopy (XPS). The binding energies were calibrated with the C1s peak at 284.6 eV. The positions of the peaks and areas under the curves were optimized by XPS Peak Fit software.

2.3. Electrochemical characterization

Electrochemical properties were characterized by CR2032 coin cells at room temperature. The positive electrodes of samples were consisted of mixtures slurry with active materials (80 wt%), acetylene black (Super-P) (10 wt%), polyvinylidene fluoride (PVDF) binder (10 wt%) dissolving in N-methyl-2-pyrrolidinone (NMP). After thoroughly stirred, the mixture slurry was pressed uniformly on an aluminum

foil current collector, then dried in the vacuum oven at 110 ℃ overnight to remove the NMP solvent before use. The electrode was punched to 14 mm diameter round discs, and then assembled the cathode coin cells with metallic lithium as counter electrode, a polypropylene porous film Celgard 2400 as separator, 1 M $LiPF_6$ (EC/DEC = 1:1 in volume) as electrolyte solution in an Ar-filled dry glove box. Galvanostatic charge-discharge tests were measured between 2.0 and 4.8 V vs. Li/Li^+ using a Land-CT2001 (Jinnuo Wuhan, China) battery test system at room temperature (~25 ℃) and 50 ℃ at a constant current density of 20 mA g^{-1}. The rate performances were completed at a different current density of 20, 100, 200, 400, 600 mA g^{-1} in the voltage range of 2.0-4.8 V at room temperature.

3. Results and discussion

3.1. XRD and XPS structural characterization

XRD patterns of undoped and Zr^{4+}substituted samples are showed in Fig.1(a). XRD patterns suggest all samples have a high degree of crystallization because all diffraction peaks are sharp and well-defined. The strong peaks indicate a typical layered hexagonal α-$NaFeO_2$ structure with a R-3m space group, as the previous studies proved [33, 34]. The weak peaks in the 2θ range of 20-25 ° are features of the monoclinic unit cell C2/m symmetry, owing to a $LiMn_6$ cation arrangement, which are similar to that occurred in Li_2MnO_3. As shown in Fig.1(b), the superlattice peaks become slightly broad as the increase of Zr content, suggesting that the superlattice feature are influenced by Zr doping. As to the main diffraction peaks of Zr^{4+}

substituted samples, their patterns are consistent with the undoped cathode materials, except for Zr10% samples, which contains some minor residual peaks of Li_2ZrO_3 marked by rectangles in Fig.1(c). Nevertheless, as shown in Fig.1(d), the diffraction peaks slightly move to lower angles as the increase in Zr^{4+} content, indicating that Zr^{4+} ions are doped into the lattice and make the expansion of unit cell volume[32]. We believe that it should be related to the lager ionic radius of Zr^{4+} (rZr^{4+} = 0.072 nm) than that of Mn^{4+} (rMn^{4+} = 0.053 nm) and Ni^{2+} (rNi^{2+} = 0.069 nm). However, when the Zr^{4+} doping content is more than 4%, the diffraction peaks almost do not move compared with the undoped sample. It is probably due to the lager ionic radius of Zr^{4+} can not get into the crystal structure. Because when the doping content is 10%, it can form Li_2ZrO_3 phase.

The I_{003}/I_{104} ratio value is carried out by Jade 5.0 software and the result is showed in Table 1. As shown in Table 1, the integrated intensity ratio of I_{003}/I_{104} , which represents the degree of cation mixing of Ni^{2+} and Li^{+} ions in the layered structure, gradually drops down as the increase in Zr^{4+} content, suggesting the degree of the cation mixing is increasing [35]. According to the published papers, it is negligible to consider the cation mixing, when the I_{003}/I_{104} value is > 1.2[36].

The valence states of Ni, Co, and Mn, Zr ions in the samples are tested by X-ray photoelectron spectroscopy (XPS). The main binding energies of $Co2p_{3/2}$, $Mn2p_{3/2}$, $Zr3d_{5/2}$ peaks are closed to 780.3 eV, 654.1 eV, 182.0 eV, respectively (they are not shown here), which is consistent with the values in Ref [37-40], indicating the valence of Co, Mn, Zr in the samples are trivalent, tetravalent, tetravalent, respectively. Fig.2

shows the main binding energies of $Ni2p_{3/2}$ peak for all samples. They shift from a lower binding energy of 854.70 eV to a higher binding energy of 855.64 eV as the increase in Zr^{4+} content and the relative Ni^{2+}/Ni^{3+} contents are gradually getting smaller from 1.37 to 1.25 in Table S1 (supplementary data), suggesting that Ni^{2+} is partly oxidized to Ni^{3+} in doped samples. Fig.S3 (supplementary data) shows the main binding energies of O 1s peak for all samples. From Fig.S3, the peaks around 529.0 and 530.0 eV are assigned to O^{2-} anions. The peaks around 531.0 and 532 eV are assigned to NiO compounds [41] and Ni_2O_3 compound [42]. Due to the existence of Ni^{3+}, the intensity of peak around 531.0 and 532 eV in the Zr doped samples is higher than that in the undoped sample [43]. These results suggest that the minor decrease in the unit cell volume when the Zr content is more than 4% should be originate from the oxidation of Ni^{2+} (rNi^{2+} = 0.069 nm) to Ni^{3+} (rNi^{3+} = 0.06 nm). Moreover, according to the published result, the level of Li^{+}/Ni^{2+} disordering increases with the decrease of Ni^{2+} content [44]. These results are consistent well with the change in the I_{003}/I_{104} ratio value mentioned above in our structural analysis.

3.2. Electrochemical Performances

Fig.3 shows the initial charge-discharge curves and cycle performances of $0.6Li[Li_{1/3}Mn_{2/3(1-x)}Zr_{2/3x}]O_2$ $0.4LiMn_{5/12}Ni_{5/12}Co_{1/6}O_2$ ($0 \leq x \leq 10\%$) at a current density of 20 mA g^{-1} between 2.0-4.8 V at room temperature (RT). As to the initial charge curve, it exhibits a slope region (3.7-4.5 V) and a long plateaus (> 4.5 V) related to two kinds of lithium de/insertion process. Moreover, the slope region is

ascribed to Li^+ ions extraction from $LiMn_{5/12}Ni_{5/12}Co_{1/6}O_2$ layer with oxidation-reduction reactions of Ni^{2+}/Ni^{4+} and Co^{3+}/Co^{4+}. The long plateau is regarded as the release of oxygen removing Li_2O from Li_2MnO_3 layered structure, which results in an irreversible electrochemical activation reaction [6, 45]. As shown in Table 2, the practical charge capacities of Zr^{4+} substituted materials are higher than the theoretical value (314.9 mA h g^{-1}) except for Zr10% materials. This suggests all of Zr doped samples can efficiently increase the capacity and reduce the irreversible capacity loss. Among them, Zr4% doped samples present the highest first discharge capacity of 261 mA h g^{-1}, with the highest first coulombic efficiency of 80%. Its irreversible capacity loss value is only 65.2 mA h g^{-1} , much lower than the undoped samples. After 100 cycles at 20 mA g^{-1}, the discharge capacity of undoped samples drop to 168.6 mA h g^{-1} with a capacity retention of 72%, as shown in Fig.3 (b). In the case of the Zr2% doped samples and Zr4% doped samples, the reversible capacities are 220.7, 218.9 mA h g^{-1} and the capacity retention is 86% and 84%, respectively, higher than those of the undoped samples. These results suggest Zr doping could improve the electrochemical properties. It has reported that Zr-O bond energy is higher than that of Mn-O bond [46,47]. We believed that the substitution of Zr for Mn can stabilized the structure during the charge and discharge process and this should be related to the improvement of cyclic performances. As to other samples, the discharge capacities of Zr6%, Zr8%, Zr10% turn to 167.5, 182.5, 174.7 mA h g^{-1} with a capacity retention of 68%, 77%, 79%, respectively. We believed that the decrease in the

reversible capacity should be attributed to the increase in the Zr content since Zr is electrochemical inert during the cycling.

Fig.4 describes the charge/discharge voltage profiles of 1, 30, 50, 70, 90 cycles at a current density 20 mA g^{-1} for $0.6Li[Li_{1/3}Mn_{2/3(1-x)}Zr_{2/3x}]O_2$ $0.4LiMn_{5/12}Ni_{5/12}Co_{1/6}O_2$ ($0 \leq x \leq 10\%$), aiming to study the change of voltage and energy density by Zr doping. As shown in Fig.4, Zr4% doped samples show the lowest voltage change with the increasing cycle numbers compared with the undoped samples [6, 32]. (Charge midpoint voltage (CV) and discharge midpoint voltage (DV) are obtained by averaging the voltage column of the charge curve and discharge curve in origin software. Δ DV is regarded as the difference between the DV of the first discharge curve and the DV of the 99th cycle discharge curve. Δ CV is regarded as the difference between the CV of the second charge curve and the CV of the 99th cycle charge curve.) Table 3 shows Δ DV and Δ CV of undoped and doped samples. From Table 3, Zr4% doped samples reveal Δ DV is 0.15 V. While for the undoped samples, Δ DV is 0.31 V, twice as much as Zr4% doped samples. Meanwhile, Zr4% doped samples show Δ CV is 0.15 V, triple as much as the undoped samples. This significantly reveals Zr4% samples can reduce the irreversible capacity loss during cycles, due to the existence of Zr in crystal structure, which can compensate the loss of oxygen vacancies and stabilize the layered structure. Moreover, Zr2%, Zr6%, Zr8%, Zr10% samples show the slightly improvement, which is consistent with the result of cycle performances. These results suggest that Zr doping could significantly stabilize the layered structure and suppress the voltage drop during cycling. To the best of our

knowledge, this is the first report to quantitatively illustrate the voltage drop problems during the cycling.

The rate performances of $0.6Li[Li_{1/3}Mn_{2/3(1-x)}Zr_{2/3x}]O_2$ $0.4LiMn_{5/12}Ni_{5/12}Co_{1/6}O_2$ ($0 \leq x \leq 10\%$) are shown in Fig.5 at the voltage range of 2-4.8 V at room temperature. The electrode materials are charged at 20 mA g^{-1}, then discharged at 20, 100, 200, 400, 600 mA g^{-1}, again at 20 mA g^{-1}, respectively. Although the initial discharge specific capacity of undoped samples is 247.3 mA h g^{-1} at a current density of 20 mA g^{-1}, its discharge specific capacity is 151.4 mA h g^{-1} at a high rate density of 600 mA g^{-1} with a capacity retention of 60%. For Zr2%, Zr4%, Zr6%, Zr8%, Zr10% doped samples, its initial discharge specific capacity is 269.1, 270.7, 250.9, 250.1, 216.9 mA h g^{-1}, respectively. Moreover, its discharge specific capacity at a high rate density of 600 mAg^{-1} is 154.9, 162.6, 145.5, 153.5, 143.9 mA h g^{-1} with a capacity retention of 58%, 60%, 58%, 61%, 66%, respectively. These results suggest different amount of Zr^{4+} doping samples get a relative stabilize capacity at high rates compared with the undoped samples. Combining with the cycle performance patterns (Fig.3(b)), it is believed that suitable amount of Zr^{4+} doping samples can improve the structural stability and electrochemical properties, which is benefit from the enlarge of interlayer space, making Li^+ ions extraction/insertion unimpeded during cycling.

3.3. SEM and TEM morphology features

Fig.6 shows SEM images of the undoped and the dopant Zr samples. As it can be seen, the particles of all samples are crystallized and homogeneous with a little

aggregation as the increase in Zr^{4+} content. And the particle size of all samples are about 100-500 nm in diameter.

Fig.7 describes the TEM images of undoped samples and Zr4% doped samples before cycle and after 100 cycles at a current density of 20 mAg^{-1}, respectively. (Zr0%, Zr4% represents before cycle. Zr0%-101, Zr4% represents after 100 cycles) From Fig.S8 (supplementary data), the particle size of samples is agreement with the SEM images. Meanwhile, the grain surface of undoped sample and Zr4% doped sample is smooth before cycle in Fig.7(a), 7(b). After 100 cycles, some amorphous layers are observed on the surface of both samples as marked by arrows in Fig.7(c), 7(d), respectively. Nevertheless, its thickness of the Zr4% doped samples is about 6 nm, smaller than that of the undoped samples, whose thickness is about 17 nm. These results indicates Zr doping could significantly suppress the side reactions occurring between the electrode and electrolyte interface.

The HRTEM images and its part IFFT patterns of undoped and Zr4% samples before and after cycles are clearly shown in Fig.8. (IFFT is obtained by inversing FFT. FFT is obtained by choosing part HRTEM images via GatanDM software.) From Fig.8(0a), 8(4a), both samples present the distinct lattice fringes and the interplanar space of layered structure is 0.47 nm before cycling, revealing both samples have good crystallinity. Moreover, closer observation of lattice fringes about the dot arrays consist of rectangular and parallelogram shapes in Fig.8(0a), 8(4a), which suggests different stacking sequence of lithium ions. Parallelogram shapes facilitate the lithium ions insertion and extraction in Zr^{4+} doping samples compared with the undoped

samples, as previous report studied [48]. It appears amorphous region and disordered arrangements of lattice fringes on the surface of undoped samples in Fig.8(b), 8(0a1), which makes it form the stacking faults during subsequence cycling [49]. For the dopant Zr4%-101 samples, it shows little disordered arrangements of lattice fringes in Fig.8(4a1), which means suitable content of Zr doping could prevent the microstructural change during cycling [50].

To further elucidate the microstructural evolution after cycling, the SAED patterns of both samples are shown in Fig.9(E), 9(F). From Fig.9(E), 9(F), both samples show the presence of superlattice Li_2MnO_3 phase before cycle. We re-draw them using ✕ marks presenting the bright dot, and ∘and •marks presenting the dark dot and the disorder dot, respectively. As shown in Fig.9(Ea1), 9(Fa1), some ✕ marks disappear while some ∘marks appear, suggesting Zr^{4+} ions are merged into the crystal structure and changed its microstructure. After 100 cycles, many ✕ marks disappear and some • marks present in the case of undoped samples, as depicted in Fig.9(Ea2). These results suggest that, a severe microstructural rearrangement occurs after cycling. We believe that this rearrangement should be closely related to the voltage depression after electrochemical cycling. In the case of the Zr4% doped samples, its SEAD pattern changes slightly after 100 cycles, as shown in Fig.9(Fa2), suggesting its structural rearrangement is mild, not severe as much as occurred in undoped one. Therefore, Zr 4% doped sample exhibits the smallest voltage drop after 100 cycles.

Fig.10 shows the cyclic performances of all samples operated at an elevated temperature (50 ℃). As shown in Fig.10, the discharge capacities of all samples are over 260 mA h g^{-1}, much higher than those at room temperature. Zr4% doped samples show more than 300 mA h g^{-1} discharge capacity at the initial charge-discharge process, suggesting Zr4% doped samples have excellent elevated temperature properties.

Conclusions

A series of layered lithium-rich oxides $0.6Li[Li_{1/3}Mn_{2/3(1-x)}Zr_{2/3x}]O_2$ $0.4LiMn_{5/12}Ni_{5/12}Co_{1/6}O_2$ ($0 \leq x \leq 10\%$) have been successfully prepared by spray-dry method. XRD analysis shows Zr^{4+} ions are successfully doped into the lattice. HRTEM results suggest Zr^{4+} ions can stabilize the layered structural feature during cycles. Among them, Zr4% samples present superior electrochemical properties with the discharge capacity of 218.9 mA h g^{-1} after 100 cycles, a high capacity retention of 84% at 20 mA g^{-1} between 2.0 and 4.8 V. It also significantly stabilizes the layered structure and suppresses the voltage drop with the lowest voltage change of 0.15 V, twice as less as the undoped materials. Therefore, a suitable amount of Zr doping for layered lithium-rich oxides can meet the urgent demands for HEVs and EVs in the future.

Acknowlegements

This work was financially supported by the Ministry of Science and Technology of

People's Republic of China (contract number: 2010EG111015) and Science & Technology Office of Jiangsu Province (BE2013006-3).

References

1 J. M. Chen, C. H. Hsu, Y. R. Lin, M. H. Hsiao and T. K. Fey, *J. Power Sources*, 2008, **184**, 498-502.

2 B. Huang, P. F. Shi, Z. C. Liang, M. Chen and Y. F. Guan, *J. Alloys Compd.*, 2005, **394**, 303-307.

3 L. Z. Zhou, Q. J. Xu, M. S. Liu and X. Jin, *Solid State Ionics*, 2013, **249**, 134-138.

4 M. M. Thackeray, C. S. Johnson, J. T. Vaughey, N. Li and S. A. Hackney, *J. Mater. Chem.*, 2005, **15**, 2257-2267.

5 M. M. Thackeray, S. H. Kang, C. S. Johnson, J. T. Vaughey, R. Benedek and S. A. Hackney, *J. Mater. Chem.*, 2007, **17**, 3112-3125.

6 T. Ohzuku, M. Nagayama, K. Tsuji and K. Ariyoshi, *J. Mater. Chem.*, 2011, **21**, 10179-10188.

7 J. Bareno, C.H. Lei, J.G. Wen, S.-H. Kang, I. Petrov and D.P. Abraham, *Adv. Mater.*, 2010, **22**, 1122-1127.

8 B. L. Ellis, K. T. Lee and L. F. Nazar, *Chem. Mater.*, 2010, **22**, 691-714.

9 H. M. Wu, J. P. Tu, Y. F. Yuan, Y. Li, X. B. Zhao and G. S. Cao, *Scripta Materials*, 2005, **52**, 513-517.

10 L. Q. Wang, L. F. Jiao, H. Yuan, J. Guo, M. Zhao, H. X. Li and Y. M. Wang, *J. Power Sources*, 2006, **162**, 1367-1372 .

11 P. He, H. J. Yu, D. Li and H. S. Zhou, *J. Mater. Chem.*, 2012, **22**, 3680-3695.

12 J. J. Liu, J. Wang, Y. G. Xia, X. F. Zhou, Y. Saixi and Z. P. Liu, *Mater. Res. Bull*, 2012, **47**, 807-812.

13 A. Ito, K. Shoda, Y. Sato, M. Hatano, H. Horie and Y. Ohsawa, *J. Power Sources*, 2011, **196**, 4785-4790.

14 J. L. Liu, M. Y. Hou, J. Yi, S. S. Guo, C. X. Wang and Y. Y. Xia, *Energy Environ. Sci.*, 2014, **7**, 705-714.

15 J. R. Croy, K. G. Gallagher, M. Balasubramanian, Z. Chen, Y. Ren, D. Kim, S.-H. Kang, D. W. Dees and M. M. Thackeray, *J. Phys. Chem. C*, 2013, **117**, 6525-6536.

16 D. Mohanty, A. S. Sefat, J. L. Li, R. A. Meisner, A. J. Rondinone, E. A. Payzant, D. P. Abraham, D. L. Wood III and C. Daniel, *Phys. Chem. Chem. Phys.*, 2013, **15**, 19496-19509.

17 N. Tran, L. Croguennec, M. Menetrier, F. Weill, Ph. Biensan, C. Jordy and C. Delmas, *Chem. Mater.*, 2008, **20**, 4815-4825.

18 B. L. Cushing and J. B. Goodenough, *Solid State Sci.*, 2002, **4**, 1487-1493.

19 N. Yabuuchi, K. Yoshii, S.-T. Myung, I. Nakai and S. Komaba, *J. Am. Chem. Soc.*, 2011, **133**, 4404-4419.

20 Z. Y. Wang, E. Z. Liu, L. C. Guo, C. S. Shi, C. N. He, J. J. Li and N. Q. Zhao, *Surface & Coatings Technology*, 2013, **235**, 570-576.

21 S. J. Shi, J. P. Tu, Y. Y. Tang, X. Y. Liu, Y. Q. Zhang, X. L. Wang and C. D. Gu, *Electrochimica Acta*, 2013, **88**, 671- 679.

22 X. Y. Liu, T. Huang and A. Yu, *Electrochimica Acta*, 2015, **163**, 82-92.

23 H. J. Yu and H. S. Zhou, *J. Mater. Chem.*, 2012, **22**, 15507-15510.

24 J. C. Knight, P. Nandakumar, W. H. Kanb and A. Manthiram, *J. Mater. Chem. A.*, 2015, **3**, 2006-2011.

25 X. Jin, Q. J. Xu, H. M. Liu, X. L. Yuan and Y. Y. Xia, *Electrochimica Acta*, 2014, **136**, 19-26.

26 X. Y. Liu, T. Huang and A. Yu, *Electrochimica Acta*, 2014, **133**, 555-563.

27 Y. Zang , C. X. Ding , X. C. Wang, Z. Y. Wen and C. H. Chen, *Electrochimica Acta*, 2015, **168**, 234-239.

28 J. H. Park, J. S. Lim, J. G. Yoon, K. S. Park, J. H. Gim, J. J. Song, H. S. Park, D. M. Im, M. S. Park, D. C. Ahn, Y. K. Paik and J. K. Kim, *Dalton Trans.*, 2012, **41**, 3053-3059.

29 S. F. Kang, H. F. Qin, Y. Fang, X. Li and Y. G. Wang, *Electrochimica Acta*, 2014, **144**, 22-30.

30 T. Akita, M. Tabuchi, Y. Nabeshima, K. Tatsumi and M. Kohyama, *J. Power Sources*, 2014, **254**, 39-47.

31 S. H. Kang and K. Amine, *J. Power Sources*, 2005, **146**, 654-657.

32 S. H. Wang, Y. X. Li, J. Wu, B. Z. Zheng, M. J. McDonald and Y. Yang, *Phys. Chem. Chem. Phys.*, 2015, **17**, 10151-10159.

33 J. L. Liu, J. Wang and Y. Y. Xia, *Electrochim Acta*, 2011, **56**, 7392-7396.

34 G.-Z. Wei, X. Lu, F.-S. Ke, L. Huang, J. T. Li, Z.-X. Wang, Z.-Y. Zhou and S.-G. Sun, *Adv. Mater.*, 2010, **22**, 4364-4367.

35 W. B. Hua, J. B. Zhang, Z. Zheng, W. Y. Liu, X. H. Peng, X.-D. Guo, B. H. Zhong, Y.-J. Wang and X. L. Wang, *Dalton Trans.*, 2014, **43**, 14824-14832.

36 W. He, J. F. Qian, Y. L. Cao, X. P. Ai and H. X. Yang, *RSC Adv.*, 2012, **2**, 3423-3429.

37 H. W. Guo, Z. D. Peng, Y. B. Cao and G. R. Hu, *Electrochimica Acta*, 2013, **90**, 350-357.

38 Y. W. Tsai, J. F. Lee, D. G. Liu and B. J. Hwang, *J. Mater. Chem.*, 2004, **14**, 958-965.

39 Y. Huang, J. Chen, J. Ni, H. Zhou and X. Zhang, *J. Power Sources*, 2009, **188**, 538-545.

40 Z. Y. Wang, E. Z. Liu, L. C. Guo, C. S. Shi, C. N. He, J. J. Li and N. Q. Zhao, *Surface & Coatings Technology*, 2013, **235**, 570-576.

41 Y.J. Mai, J.P. Tu, X.H. Xia, C.D. Gu and X.L. Wang, *J. Power Sources*, 2011, **196,** 6388-6393.

42 R. Molaei, R. Bayati and J. Narayan, *Cryst. Growth Des.*, 2013, **13,** 5459-5465.

43 Y.T. Zhang, P.Y. Hou, E.L. Zhou, X.X. Shi, X.Q. Wang, D.W. Song, J. Guo and L.Q. Zhang, *J. Power Sources*, 2015, **292,** 58-65.

44 F. Wu, J. Tian, Y. F. Su, J. Wang, C. Z. Zhang, L. Y. Bao, T. He, J. H. Li and S. Chen, *ACS Appl. Mater. Interfaces*, 2015, **7**, 7702-7708.

45 C. S. Johnson, J-S. Kim, C. Lefief, N. Li, J. T. Vaughey and M. M. Thackeray, *Electrochemistry Communications*, 2004, **6**, 1085-1091.

46 Q. X. Du, Z. F. Tang, X. H. Ma, Y. Zang, X. Sun, Y. Shao, Z. Y. Wen and C. H.

Chen, *Solid State Ionics*, 2015, **279**, 11–17.

47 B. Lin, Z. Y. Wen, Z. H. Gu and X. X. Xu, *J. Power Sources*, 2007, **174**, 544–547.

48 W. W. Liu, G. Q. Fang, B. B. Xia, H. D. Sun, S. Kaneko and D. C. Li, *RSC Adv.*, 2013, **3**, 15630-15635.

49 A. Ito, D. C. Li, Y. Sato, M. Arao, M. Watanabe, M. Hatano, H. Horie and Y. Ohsawa, *J. Power Sources*, 2010, **195**, 567-573.

50 M. Gu, L. Belharouak, J. M. Zheng, H. M. Wu, J. Xiao, A. Genc, K. Amine, S. Thevuthasan, D. R. Baer, J. G. Zhang, N. D. Browning, J. Liu and C. M. Wang, *ACS Nano*, 2013, **7**, 760-767.

Table and figure images

Table 1 I(003)/I(104) in $0.6Li[Li_{1/3}Mn_{2/3(1-x)}Zr_{2/3x}]O_2$ $0.4LiMn_{5/12}Ni_{5/12}Co_{1/6}O_2$ ($0 \leq x \leq 10\%$) with different Zr amount

Table 2 Electrochemical data of all samples at first charge-discharge at a current density of 20 mA g^{-1}.

Table 3 The difference of midpoint discharge voltage (ΔDV) between 1cycle and the 99th cycle. the difference of midpoint charge voltage (ΔCV) between 2nd cycle and 99th cycle

Fig.1. （ a ） X-ray diffraction patterns of $0.6Li[Li_{1/3}Mn_{2/3(1-x)}Zr_{2/3x}]O_2$ $0.4LiMn_{5/12}Ni_{5/12}Co_{1/6}O_2$ ($0 \leq x \leq 10\%$) samples and its magnified areas in the 2θ range of (b) 20-22 °, (c) 35-44 °, (d) 18.4-19 °.

Fig.2. XPS patterns for Ni 2p in $0.6Li[Li_{1/3}Mn_{2/3(1-x)}Zr_{2/3x}]O_2$ $0.4LiMn_{5/12}Ni_{5/12}Co_{1/6}O_2$ ($0 \leq x \leq 10\%$) samples.

Fig.3. (a) The first charge and dicharge profile vs. Voltage and (b) cycling performances of $0.6Li[Li_{1/3}Mn_{2/3(1-x)}Zr_{2/3x}]O_2$ $0.4LiMn_{5/12}Ni_{5/12}Co_{1/6}O_2$ (x = 0, x = 2%, x = 4%, x = 6%, x = 8%, x = 10%) samples at a current density of 20 mA g^{-1} between 2-4.8 V at RT.

Fig.4. The 1st, 30th, 50th, 70th and 90th charge/discharge voltage profiles of $0.6Li[Li_{1/3}Mn_{2/3(1-x)}Zr_{2/3x}]O_2$ $0.4LiMn_{5/12}Ni_{5/12}Co_{1/6}O_2$ (x = 0, x = 2%, x = 4%, x = 6%, x = 8%, x = 10%) samples at a current density of 20 mA g^{-1} between 2-4.8 V.

Fig.5. Rate performances of $0.6Li[Li_{1/3}Mn_{2/3(1-x)}Zr_{2/3x}]O_2$ $0.4LiMn_{5/12}Ni_{5/12}Co_{1/6}O_2$ (x = 0, x = 2%, x = 4%, x = 6%, x = 8%, x = 10%) samples between 2-4.8 V.

Fig.6. SEM images of $0.6Li[Li_{1/3}Mn_{2/3(1-x)}Zr_{2/3x}]O_2$ $0.4LiMn_{5/12}Ni_{5/12}Co_{1/6}O_2$ (x = 0, x = 2%, x = 4%, x = 6%, x = 8%, x = 10%) samples.

Fig.7. TEM patterns of undoped and Zr4% doped samples, (a) x = 0 before cycle, (b) x = 4% before cycle, (c) x = 0 after 101cycles, (d) x = 4% after 101cycles.

Fig.8. HRTEM patterns of undoped and Zr4% doped samples, (a) x = 0 before cycle, (b) x = 0 after 101cycles, (c) x = 4% before cycle, (d) x = 4% after 101cycles. Its IFFT images, (0a) x = 0 before cycle, (0a1) x = 0 after 101cycles, (4a) x = 4% before cycle, (4a1) x = 4% after 101cycles.

Fig.9. SAED patterns of undoped and Zr4% doped samples, (E) x = 0 before and after 101cycles, (F) x = 4% before and after 101cycles. Its equivalent simulation patterns, (Ea1) x = 0 before cycle, (Ea2) x = 0 after 101cycles, (Fa1) x = 4% before cycle, (Fa2)

x = 4% after 101cycles.

Fig.10. Cycling performances of $0.6Li[Li_{1/3}Mn_{2/3(1-x)}Zr_{2/3x}]O_2$ $0.4LiMn_{5/12}Ni_{5/12}Co_{1/6}O_2$ (x = 0, x = 2%, x = 4%, x = 6%, x = 8%, x = 10%) samples at a current density of 20 mA g^{-1} between 2-4.8 V at elevated temperature (50 ℃).

Table 1 I(003)/I(104) in $0.6Li[Li_{1/3}Mn_{2/3(1-x)}Zr_{2/3x}]O_2$ $0.4LiMn_{5/12}Ni_{5/12}Co_{1/6}O_2$ ($0 \leq x \leq 10\%$) with different Zr amount

Sample	Zr0%	Zr2%	Zr4%	Zr6%	Zr8%	Zr10%
I(003)/I(104)	1.32	1.29	1.29	1.27	1.24	1.24

Table 2 Electrochemical data of all samples at first charge-discharge at a current density of 20 mA g^{-1}

Samples	First charge capacity/mA h g^{-1}	First discharge capacity/mA h g^{-1}	First coulombic efficiency/%	Irreversible capacity/mA h g^{-1}
Zr0%	308.7	232.8	75.4	75.9
Zr2%	327.2	255.8	78.2	71.4
Zr4%	326.2	261	80	65.2
Zr6%	323.9	241.4	74.5	82.5
Zr8%	316.2	237.6	75.1	78.6
Zr10%	301.5	221.7	73.5	79.8

Table 3 The difference of midpoint discharge voltage (∆DV) between 1cycle and the 99th cycle. The difference of midpoint charge voltage (∆CV) between 2nd cycle and 99th cycle

Samples	∆DV/V	∆CV/V
Zr0%	0.31	0.05
Zr2%	0.24	0.14
Zr4%	0.15	0.15
Zr6%	0.23	0.11
Zr8%	0.21	0.11
Zr10%	0.24	0.11

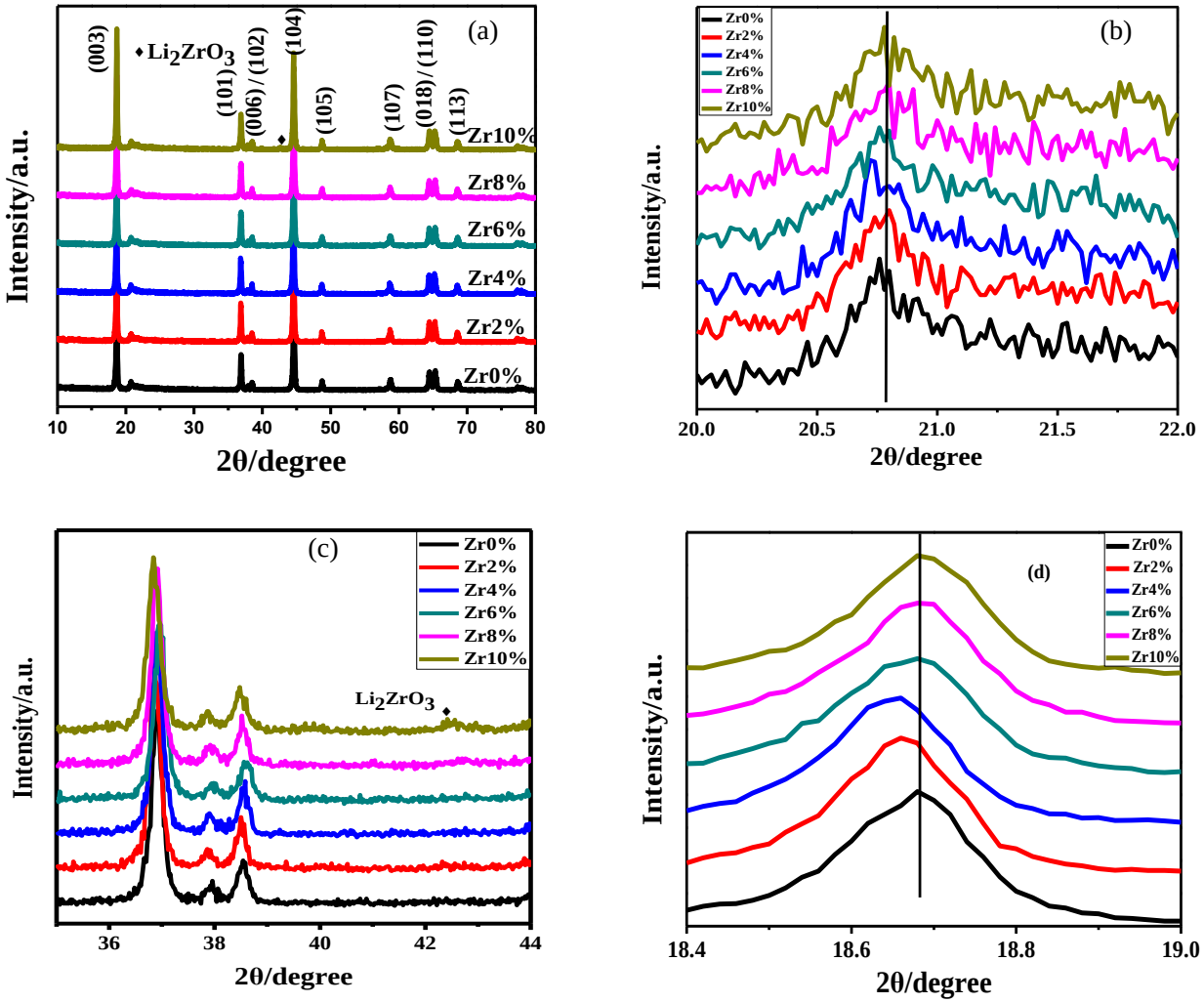

Fig.1

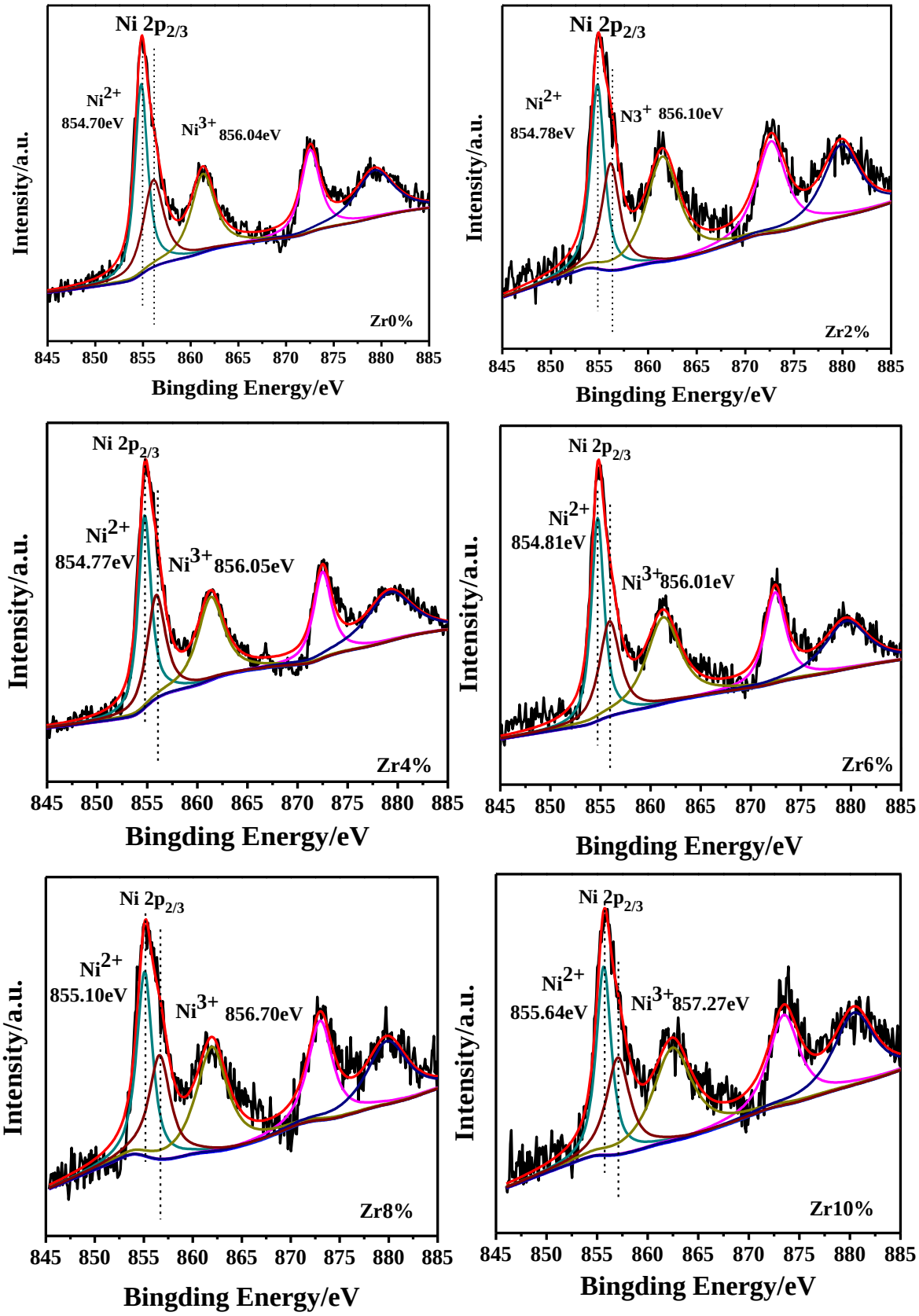

Fig.2

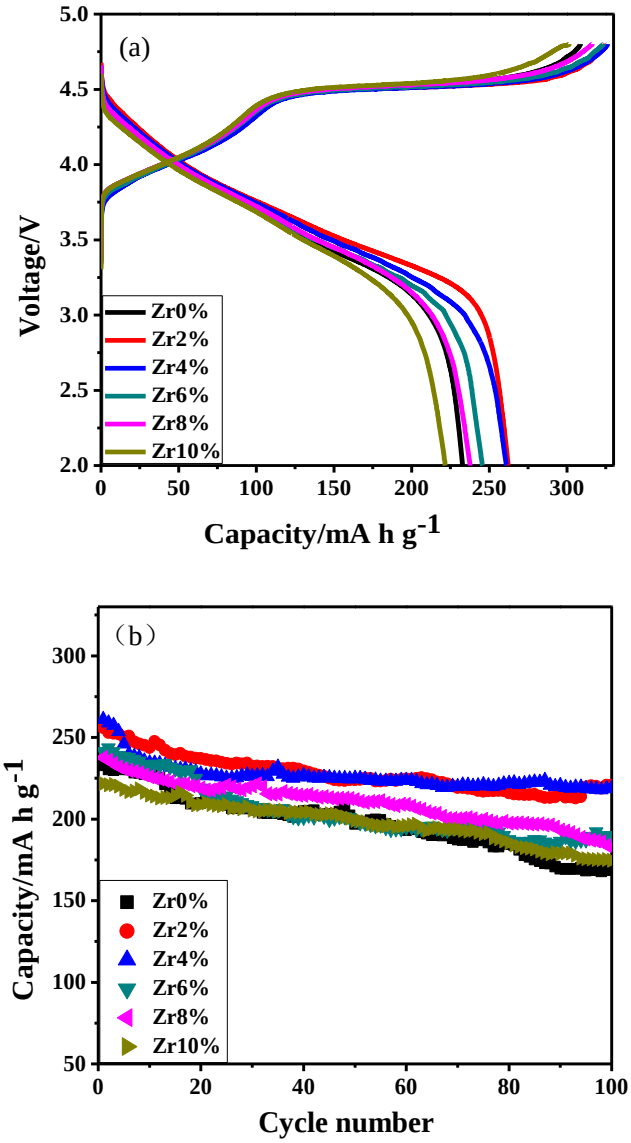

Fig.3

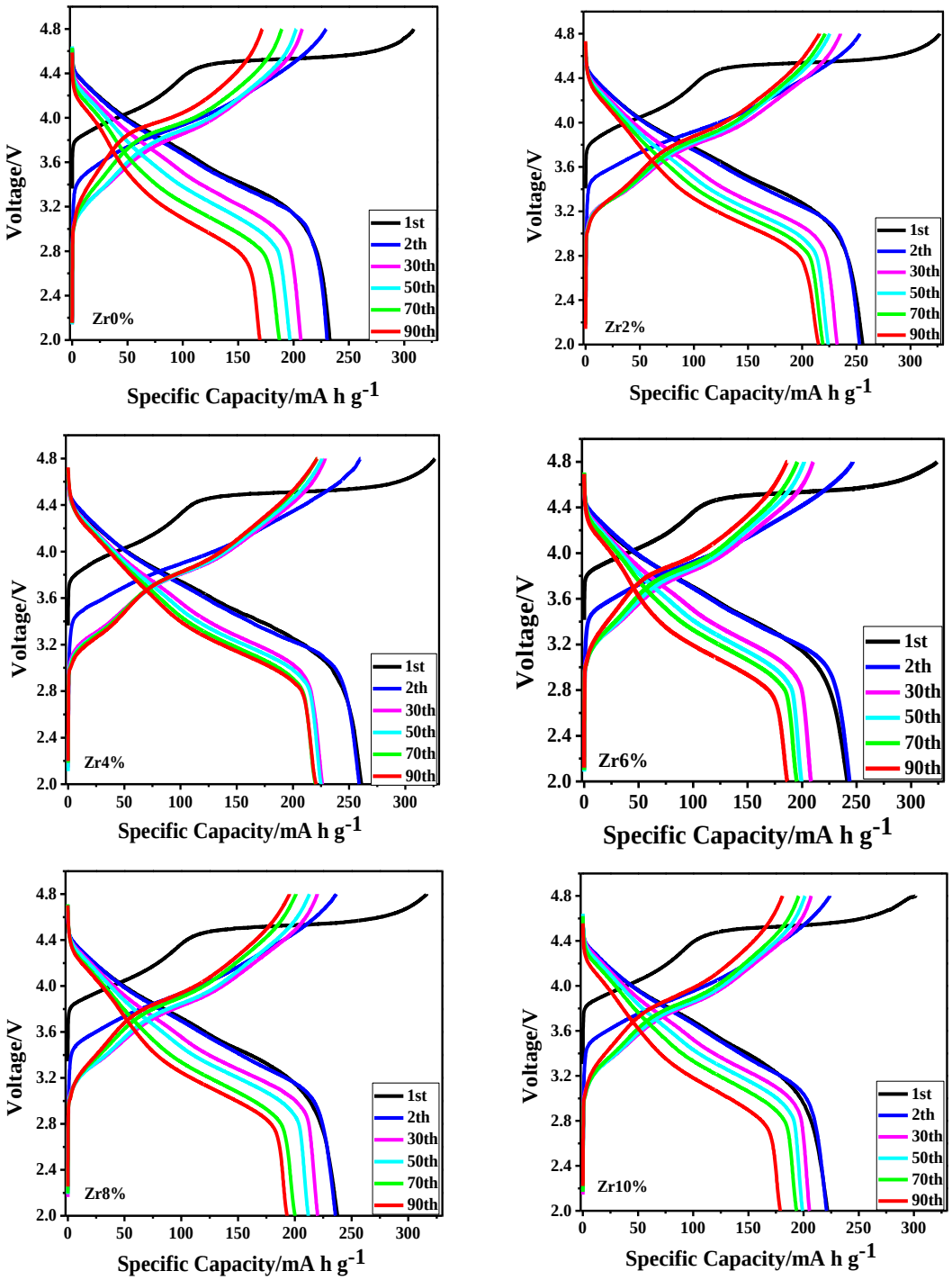

Fig.4

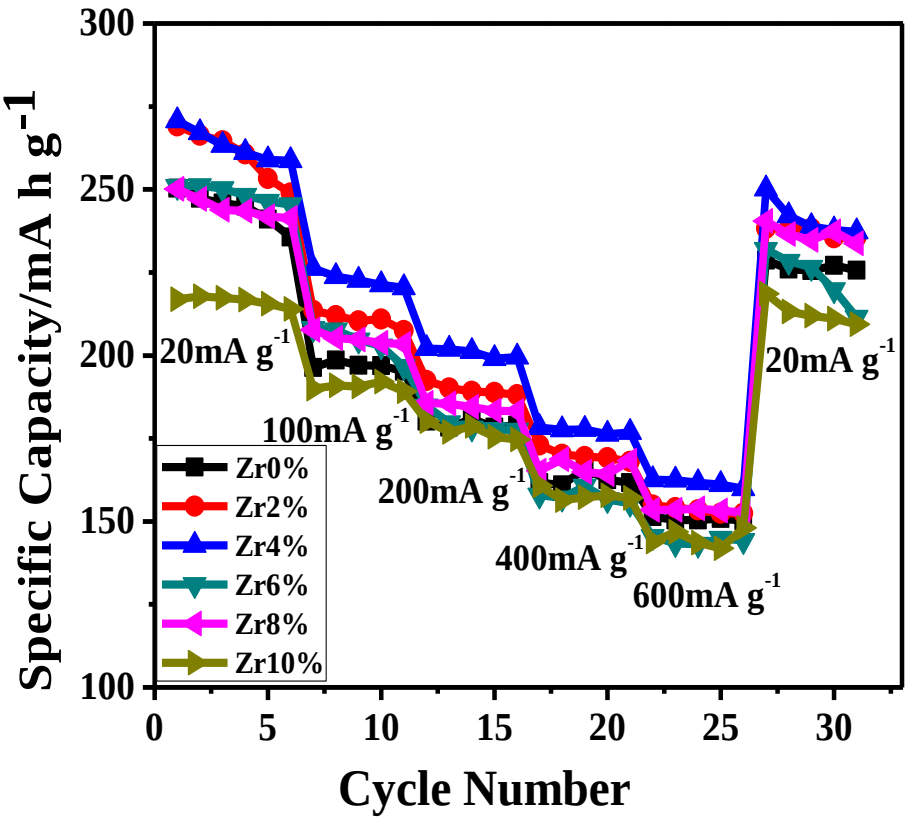

Fig.5

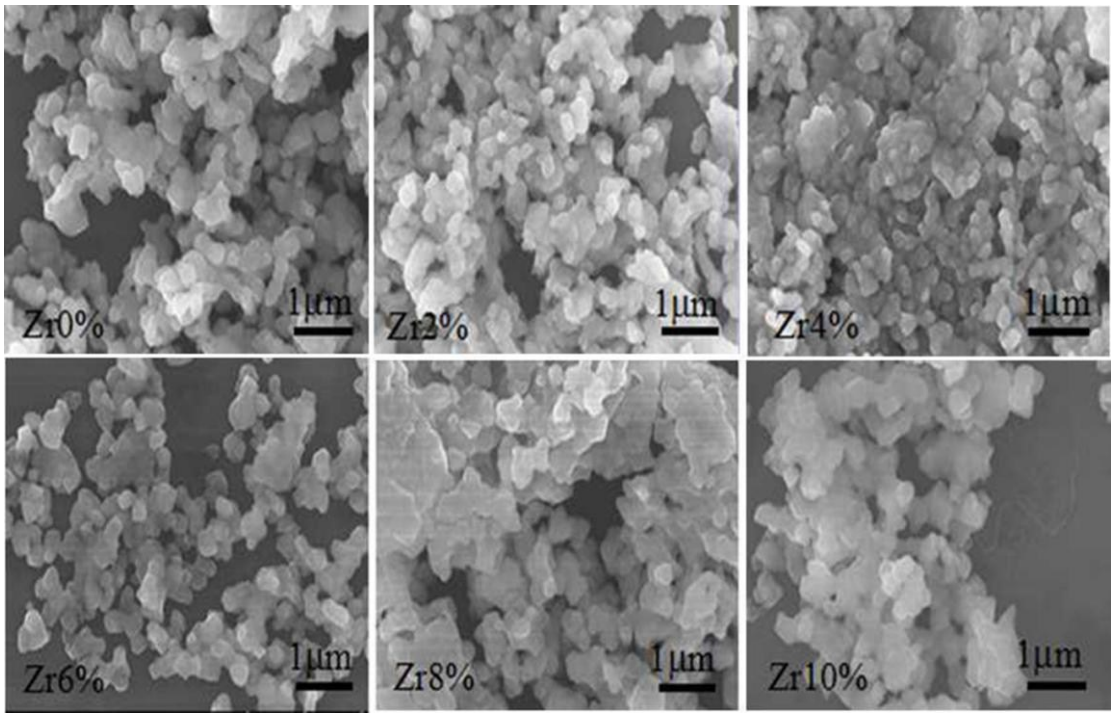

Fig.6

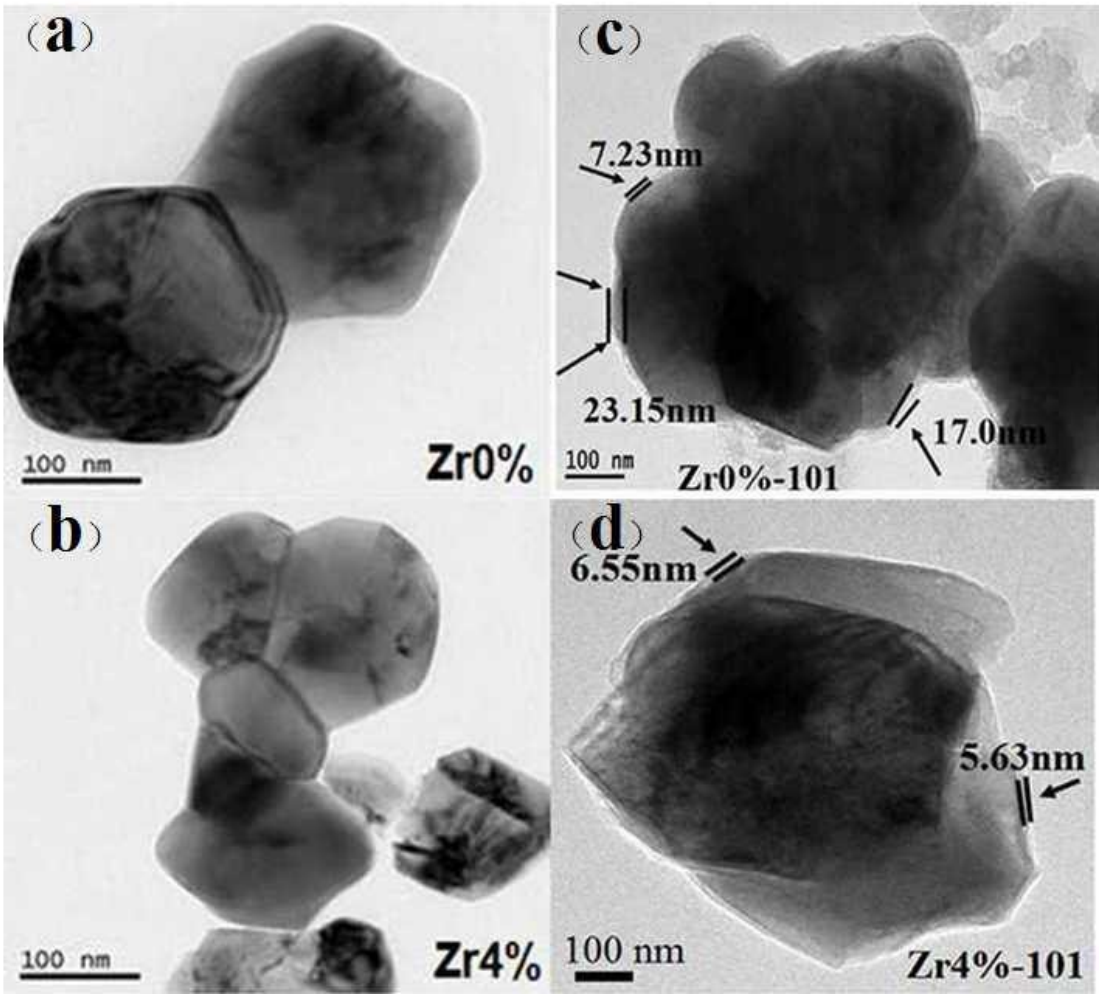

Fig.7

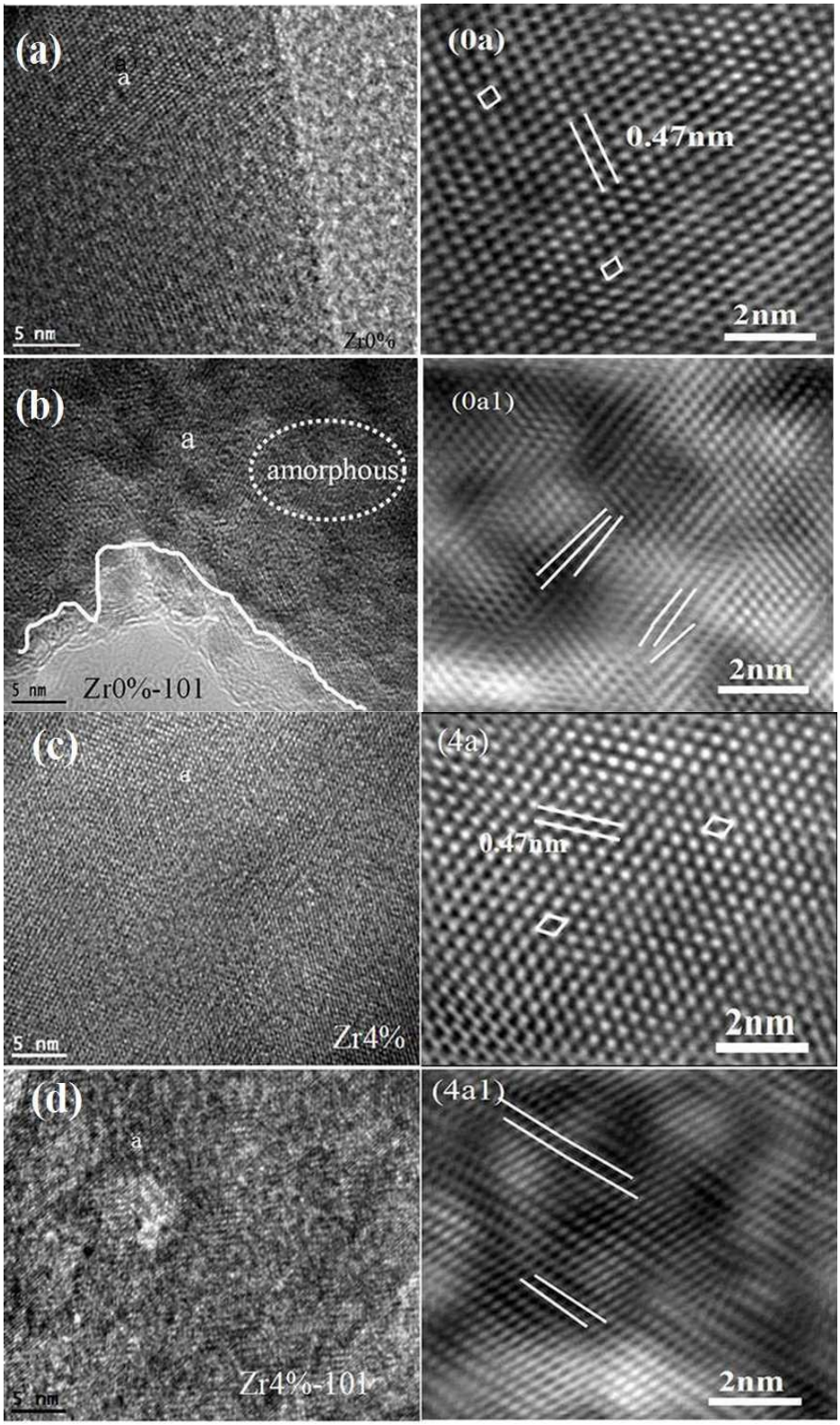

Fig.8

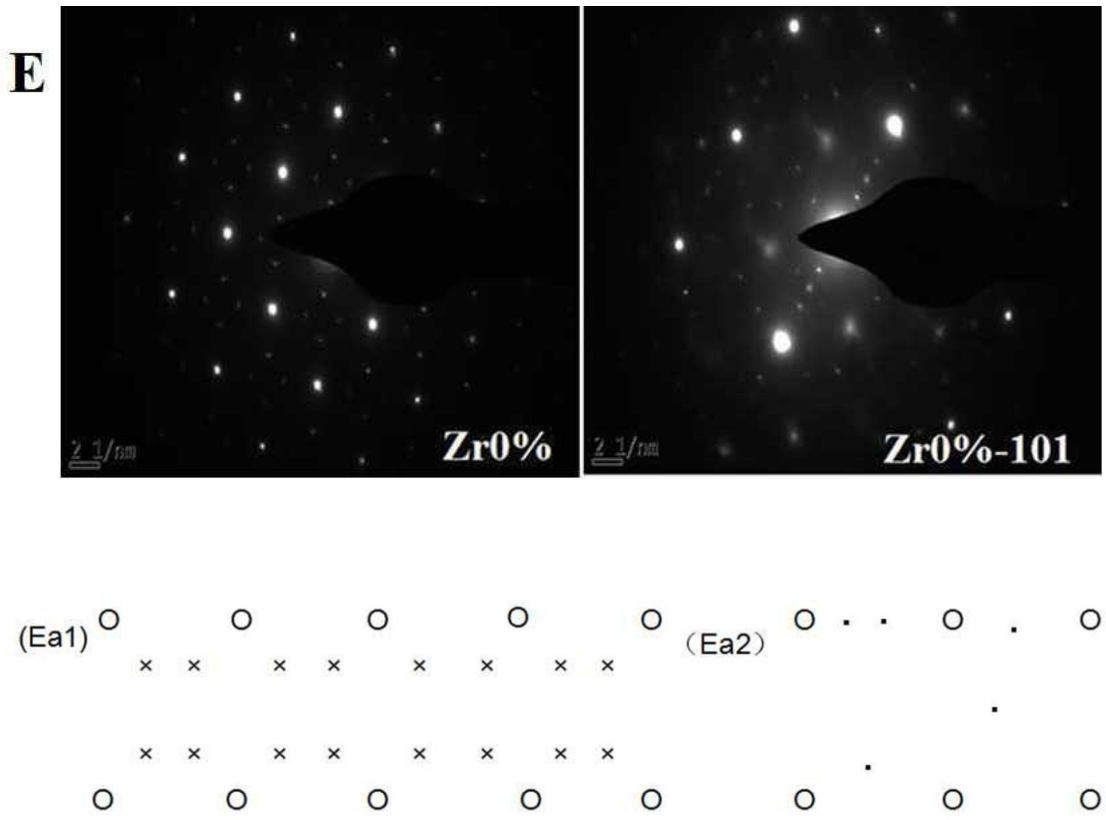

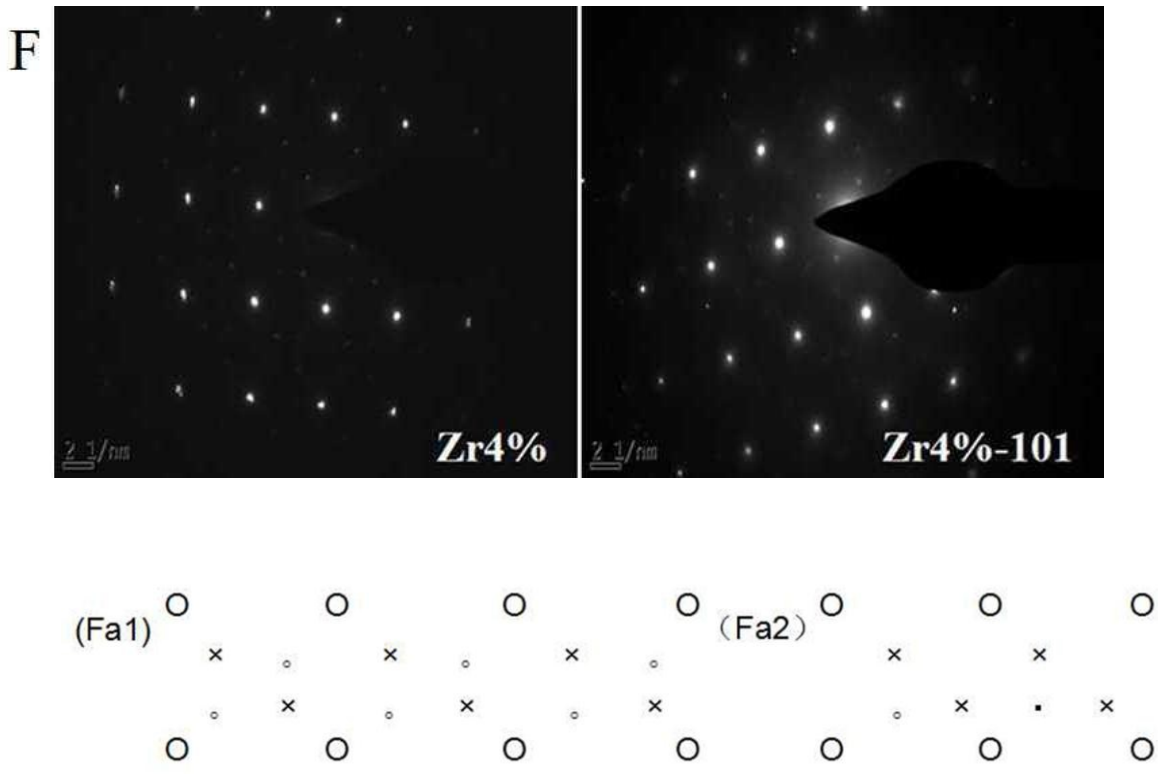

Fig.9

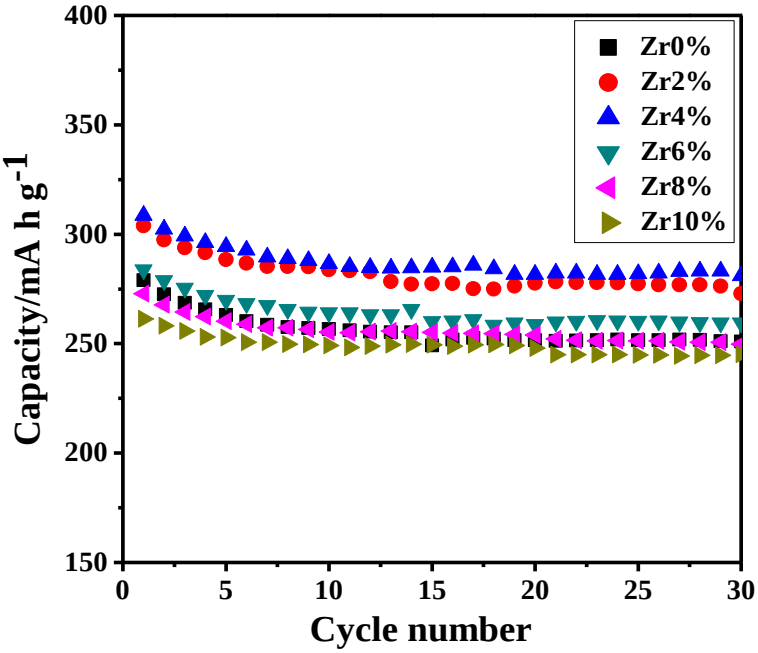

Fig.10

Graphical abstract

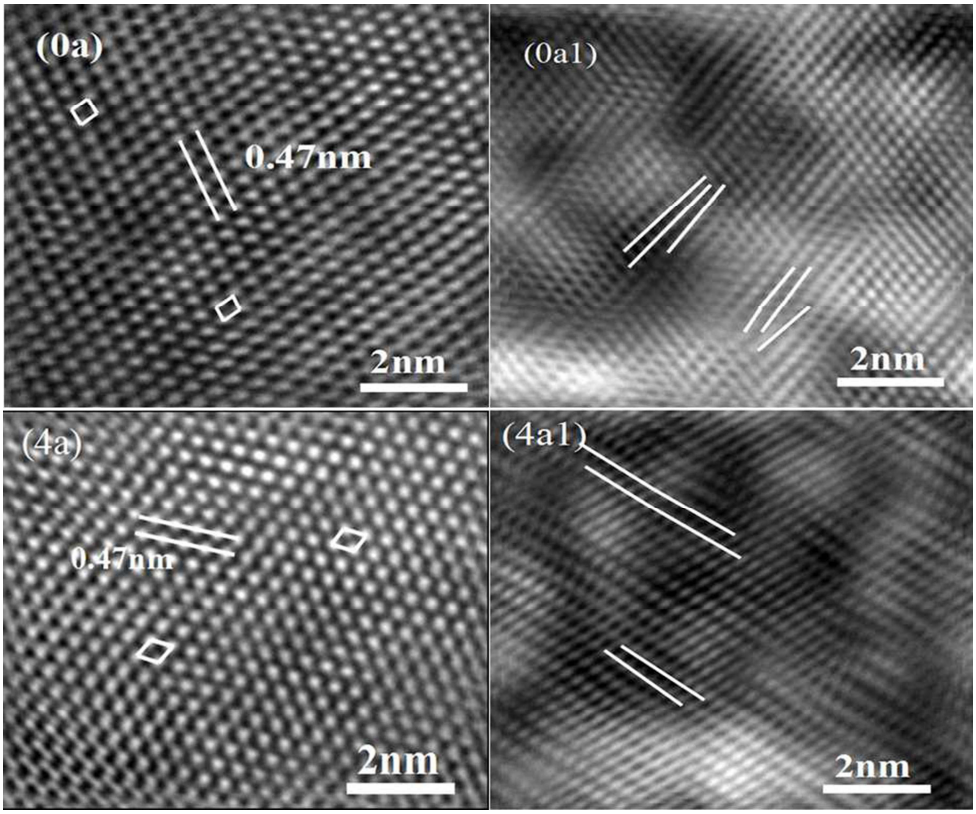

HRTEM patterns of undoped and Zr4% doped samples, (0a) x=0 before cycle, (0a1) x=0 after 101cycles, (4a) x=4% before cycle, (4a1) x=4% after 101cycles.